Research on Dynamic Characteristics of a Multi-Motor Electric Driving System Caused by Parasitic Power

Ruizhi SHU*,**, Zhengqiu XIE*, Shuaishuai GE*, Qin YIN*, Zheng ZOU*, Rulong TAN*, Jianghua FU*
*College of Mechanical Engineering, Chongqing University of Technology, Chongqing 400054, China,
E-mail: jhfu08@cqut.edu.cn (Corresponding Author)
**The State Key Laboratory Mechanical Transmissions, Chongqing University, Chongqing 400044, China
https://doi.org/10.5755/j02.mech.32097

1. Introduction

Both China and other countries have introduced a series of policies to reduce greenhouse gas emissions in dealing with climate change, and adopting electric vehicles (EVs) to replace fuel vehicles is one of the most effective measures [1]. As an important part of Evs, the electric driving system (EDS) usually consists of driving motor and mechanical structure, such as parallel shaft gear set (PSGS). In order to meet the installation space and power requirements of EVs, two or more motors are installed in the EDS to drive the EVs, forming what is called the multi-motor electric drive system (MMEDS). Besides this, the MMEDS is also used extensively in other engineering fields, such as wind energy and aerospace. In most industrial applications, permanent magnet synchronous motor (PMSM) is the best choice as driving source based on its advantages of wide speed range, high efficiency and high reliability [2]. As one of the driving types of the MMEDS, as shown in Fig.1, multiple PMSMs are often coupled together by PSGS, which produces a forced synchronization effect on the speeds of the PMSMs. Namely, when there is a rotational speed difference (RSD) between PMSMs, the speeds of PMSMs are forced to synchronize under the action of PSGS, which makes the PMSM with a fast speed will be slowed and the PMSM with a slow speed will be accelerated. As a result, the output power of the PMSM being accelerated may be decrease or even become negative; conversely, the output power of the PMSM being decelerated will increase accordingly. Staring from principle of power conservation, the output power decrement of the PMSM being accelerated is equal to the output power increment of the PMSM being decelerated. The variation in output power between PMSMs caused by RSD cause an auto excitation vibration and a variation in dynamic characteristic of MMEDS. Therefore, it is imperative to investigate the influence of the forced synchronization effect of PSGS on the dynamic characteristic of MMEDS when there is an RSD between PMSMs.

As a complex electromechanical coupling system, the dynamic characteristics of MMEDSs have attracted more and more attention and have been reported on various occasions in recent years. Li and Liu established an electromechanical coupling dynamic model (ECDM) of a nonlinear vibration machine (NVM) that driven by two motors, and then the influence of harmonic vibration synchronization control strategy on the speed difference and phase difference is discussed, the result shown that not only the dynamic response performance of NVM has been improved, but also the synchronization error (SE) between motors has

been reduced [3]. Sun et al. developed an electromechanical coupling model of a four quarter in-wheel motor suspension system and an optimization and control approach was presented to reduce the vibration of system. The results shown that the optimized model can achieve better vibration characteristics [4]. Chen presented a coupling modelling method of in-wheel motor and transient state coupling characteristics were simulated and analyzed, and the results indicated that the method can be used to provide a theoretical basis to make optimal design of a new driving in-wheel motor. [5]. Yu et al. built a dynamic model of a gear pair system driven by four motors to investigate the impact of mechanical parameters such as meshing frequency and bearing stiffness on the load transmission behaviour of each meshing gear pair, and it is pointed out that the load transmission behaviour is dependent on the bearing stiffness ratio of gear and pinions [6]. Li et al. devoted to solve the vibration issues emerged in in-wheel motors of EVs and developed an integrated model which describes the dynamic coupling process between electromagnetic excitation in motors and transient dynamic characteristic in EVs, and then the characteristics of the electromechanically motivated harassment and its coupling mechanism were discussed [7]. Wang et al. developed a dynamic model of a twin-motor coaxial series drive system of electric city bus and the influence of motor torque mutation on the vibration response was discussed, and found that the designed torque control algorithm can effectively suppress the vibration of the system [8]. Fan et al. set up a dynamic model of dual-motor coupling driving system (DCDS) and proposed an analysis method of the transmission process for the DCDS, and the influence of meshing stiffness and excitation source on the dynamic characteristics were discussed, the results shown that the effect of the dynamic meshing force was affected by the rotational speed of the dual motors and increasing the meshing stiffness can significantly reduce the vibration amplitude of the low-order vibration [9]. Wang et al. established a ECDM of the full drive trains of a differential speed regulation system including gearbox, load, motor and its inverter power supply, and the dynamic properties of the system were discussed under variable operation conditions, the results indicated that both inverter harmonics and mechanical meshing force harmonics can be observed in the electromagnetic torque and rotor speed of the motors [10]. Shu et al. developed an ECDM of a MMEDS considering gear transmission system, load, motor and its control, and then its dynamic and synchronization properties were discussed, the results demonstrated that the current can be regarded as a signal to monitor the torque and its synchronous performance, and the vibration properties of

MMEDS [11]. Kong et al. proposed a new structure of electric construction vehicles by using multi-motor and built its coupling dynamic model, the influence of the proposed driving torque distribution control method on the torque and speed response characteristics were studied, and found that the proposed MMDS with the control strategy can enhance the total efficiency in the condition of ensuring the driving force [12]. Shi et al. presented an improved relative coupling control structure for multi-motor speed synchronous driving system (MMSSDS) and the influence of the control structure on the dynamic tracking and synchronisation properties of MMSSDS were studied by changing tracking coefficient and synchronous coefficient, and the simulation and experimental results indicated that the tracking error and synchronisation error of the system have a notable improvement [13]. Yang et al. set up a dynamic model of a multi-motor torque coupling system and then the influence of the pinion speed SE and drive torque SE on the dynamic characteristic of the system were investigated, and the result shown that the influence of the pinion speed SE on the dynamic characteristic is greater than that of the drive torque SE, reducing speed SE or drive torque SE can significantly improve the load-sharing characteristic [14]. Fang et al developed a dynamic model of a multi-motor-pendulum vibration system and proposed a combined synchronous control strategy, and then the vibration characteristic of the system was discussed, and the numerical simulation indicated that a ideal vibration synchronization state of motors can be obtained by using the proposed control strategy [15].

In the above-mentioned researches on MMEDS, some scholars are concerned about the influence of mechanical parameters on its dynamic characteristics, and optimized the mechanical parameters to obtain the best dynamic characteristic of MMEDS. The other scholars paid great attention to the effect of control strategy or control method or control algorithm on its dynamic characteristics, and tried to improve the dynamic characteristics of mechanical structures in MMEDS or the synchronization characteristics of driving motors in MMEDS by means of control. However, the effect of the forced synchronization action of mechanical structure on the dynamic characteristics of MMEDS is ignored. Once there is an RSD between the motors, the speeds of motors are forced to synchronize under the forced synchronization action of mechanical structure, this may cause an auto excitation vibration caused by the change of motor speed and a variation in dynamic characteristics of MMEDS.

In this paper, a ECDM of MMEDS is set up and the influence of the forced synchronization action of parallel shaft gear set on the dynamic characteristics of MMEDS is discussed under different RSD. The organization of this paper is as follows: In Sect. 2, the ECDM of MMEDS is introduced. Then, the influence of the forced synchronization action of parallel gear set on the dynamic characteristics of MMEDS when there is an RSD between motors is discussed in Sect. 3. In the end, some conclusions are drawn in Sect. 4.

2. Electromechanical coupling dynamic model (ECDM)

In Fig. 1, the MMEDS consists of three PMSMs and a single stage PSGS. The torque or speed of PMSM can be transmitted to the corresponding pinion through the coupling. The three pinions engage with the wheel and evenly distribute along its circumference to drive the wheel. The output shaft is joined to the wheel by a spline, and the torque or speed from PMSM can ultimately be transmitted to the actuator that connects with the output shaft. Based on the structure feature and the fundamental theory of finite element, the MMEDS can be regarded as a combination of shafting element, gear meshing element, supporting element, coupling element and electric driving element, and its ECDM can be obtained by mean of the above elements.
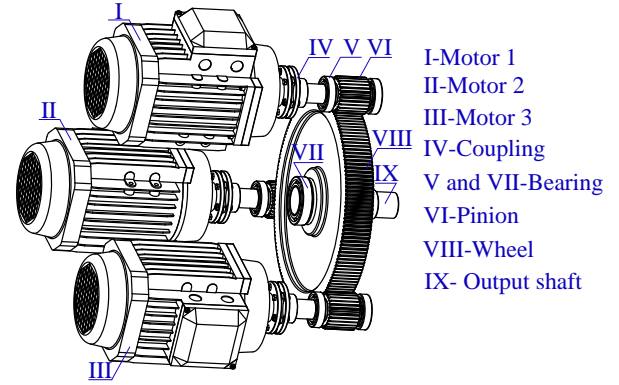

I-Motor 1
II-Motor 2
III-Motor 3
IV-Coupling
V and VII-Bearing
VI-Pinion
VIII-Wheel
IX- Output shaft

Fig. 1 3D model of MMEDS

2.1. Modelling of system constituent elements

Shafting element. From Fig. 1, it can be seen clearly that the cross-section shapes of the shafts that make up the MMEDS are all solid circle cross-section shafting elements. Therefore, the two-node Timoshenko beam element with solid circle cross-section is employed to describe the dynamic characteristic of the shafts in the MMEDS, as shown in Fig. 2. Here, l is the length of the shaft and r is the radius of the shaft. Suppose that the column vector $\mathbf{U}_{i,i+1} = [x_i, y_i, z_i, \theta_i, x_{i+1}, y_{i+1}, z_{i+1}, \theta_{i+1}]^T$ is the displacement of the corresponding nodes i and $i+1$ of the two-node Timoshenko beam element, where x_λ, y_λ and z_λ $(\lambda = i, i+1)$ represent the vibration displacement of node along x-direction, y-direction and z-direction, respectively. θ_λ $(\lambda = i, i+1)$ represents the rotational angular displacement of node around z-direction. The dynamic characteristic of two-node Timoshenko beam element can be described by the Eqs. (1) and (2):

$$\mathbf{M}_{i,i+1}\ddot{\mathbf{U}}_{i,i+1} + \mathbf{C}_{i,i+1}\dot{\mathbf{U}}_{i,i+1} + \mathbf{K}_{i,i+1}\mathbf{U}_{i,i+1} = 0. \tag{1}$$

In Eq. (1) $\mathbf{M}_{i,i+1} = diag[m_i, m_i, m_i, I_i, m_{i+1}, m_{i+1}, m_{i+1}, I_{i+1}]$ represent the mass matrix of two-node Timoshenko beam element, where m_λ and I_λ $(\lambda = i, i+1)$ are the mass and the moment of inertia of node, respectively. $\mathbf{K}_{i,i+1}$ and $\mathbf{C}_{i,i+1}$ are the stiffness and dampling matrices of two-node Timoshenko beam element respectively, and they can be written as Eq. (2) [16, 17]. In Eq. (2), E and G represents elastic modulus and shear modulus, respectively. α_1 and α_2 are the mass and stiffness proportionality coefficients, respectively. I, ξ, A and J are the cross-sectional moment of inertial, shear impact factor, cross-sectional area and polar moment of inertial, respectively, they can be expressed as Eq. (3):

$$\begin{cases} \mathbf{K}_{i,\,i+1} = \begin{bmatrix} \mathbf{K}_{11} & \mathbf{K}_{12} \\ \mathbf{K}_{21} & \mathbf{K}_{22} \end{bmatrix} \\ \mathbf{K}_{11} = \mathbf{K}_{22} = -\mathbf{K}_{12} = -\mathbf{K}_{21} \\ \mathbf{K}_{11} = \begin{bmatrix} \dfrac{12EI}{l^3(1+\xi)} & 0 & 0 & 0 \\ 0 & \dfrac{12EI}{l^3(1+\xi)} & 0 & 0 \\ 0 & 0 & AE/L & 0 \\ 0 & 0 & 0 & GJ/L \end{bmatrix}, \\ \mathbf{C}_{i,\,i+1} = \alpha_1 \times \mathbf{M}_{i,\,i+1} + \alpha_2 \times \mathbf{K}_{i,\,i+1} \end{cases} \quad (2)$$

$$\begin{cases} I = \rho\pi d^4 l / 32 \\ \xi = 12(7+6\mu)EI/6GA(1+\mu)l^2, \\ A = \pi d^2/4 \end{cases} \quad (3)$$

where: ρ and μ are the material density and Poisson's ratio, respectively.
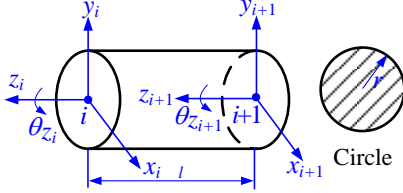
Fig. 2 Dynamic model of two-node Timoshenko element

Gear meshing element. Due to spur gear and helical gear are the most common tooth shape used in the MMEDS, without loss of generality, taking the helical gear as an example to establish the dynamic model of gear meshing element. The 3D model of a helical gear pair and its dynamic model are demonstrated in Fig. 3. The subscripts p and w are the acronyms of pinion and wheel, respectively.

$o_\lambda x_\lambda y_\lambda z_\lambda$ ($\lambda = p$ and w) is the follow-up coordinate system which is fixed on the rotation centre of gear. x_λ, y_λ, z_λ and θ_λ ($\lambda = p$ and w) are the vibration displacement along x-axis, y-axis, z-axis and the rotational angular displacement around z-axis, respectively. k_m, c_m and e_m are the meshing stiffness, meshing dampling and transmission error, respectively. r_{bp} and r_{bw} are the base radius of pinion and wheel, respectively. α, β and η are the pressure angle, helical angle and position angle of pinion, respectively. Hence, the dynamic model of a helical gear meshing element can be described as:
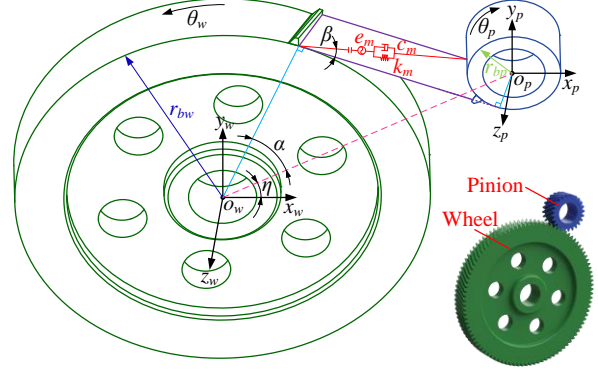
Fig. 3 3D model of gear meshing pair and dynamic model of gear meshing pair

$$\mathbf{M}_{pw}\ddot{\mathbf{U}}_{pw} + \mathbf{C}_{pw}(\dot{\mathbf{U}}_{pw} - \dot{\mathbf{e}}_{pw}) + \mathbf{K}_{pw}(\mathbf{U}_{pw} - \mathbf{e}_{pw}) = \mathbf{F}_{pw}, \quad (4)$$

where: $\mathbf{M}_{pw} = \mathrm{diag}[m_p, m_p, m_p, I_p, m_w, m_w, m_w, I_w]$ is the mass matrix of a helical gear pair. $\mathbf{K}_{pw}$, $\mathbf{C}_{pw}$, $\mathbf{e}_{pw}$, $\mathbf{U}_{pw}$ and $\mathbf{F}_{pw}$ are the meshing stiffness, meshing dampling, transmission error, vibration displacement and exciting force matrices of a helical gear meshing element. They can be described as:

$$\begin{cases} \mathbf{K}_{pw} = k_m \mathbf{V}_{pw}^T \mathbf{V}_{pw} \\ \mathbf{C}_{pw} = c_m \mathbf{V}_{pw}^T \mathbf{V}_{pw}, \quad c_m = 2\zeta\sqrt{k_m/(1/m_{eq,1} + 1/m_{eq,2})} \\ \mathbf{e}_{pw} = e_m \mathbf{V}_{pw}^T \mathbf{V}_{pw} \\ \mathbf{U}_{pw} = [x_p, y_p, z_p, \theta_p, x_w, y_w, z_w, \theta_w]^T \\ \mathbf{F}_{pw} = [F_{px}, F_{py}, F_{pz}, T_{drive}, F_{wx}, F_{wy}, F_{wz}, -T_{load}]^T \\ \mathbf{V}_{pw} = [\cos\beta\sin(\alpha\mp\eta), \cos\beta\cos(\alpha\mp\eta), \sin\beta, r_{bp}\cos\beta, \quad , \\ \quad -\cos\beta\sin(\alpha\mp\eta), -\cos\beta\cos(\alpha\mp\eta), -\sin\beta, -r_{bw}\cos\beta] \\ k_m = \bar{k}_m + \sum_{j=1}^{7} \hat{k}_{mj} \cdot \cos\left(\dfrac{j\cdot 2\pi\cdot r_{bp}\cdot\theta_p}{p_{bp}} + \gamma_i\right) \\ e_m = \bar{e}_m + \sum_{j=1}^{7} \hat{e}_{mj} \cdot \cos\left(\dfrac{j\cdot 2\pi\cdot r_{bp}\cdot\theta_p}{p_{bp}} + \gamma_i\right) \end{cases} \quad (5)$$

where: $\mathbf{V}_{pw}$ is the helical gear pair meshing matrix. $\bar{k}_m$, $\hat{k}_{mj}$ and $\bar{e}_m$, $\hat{e}_{mj}$ are the average meshing stiffness, j^{th} harmonic amlitude of meshing stiffness and the average transmission error, j^{th} harmonic amlitude of trransmission error, respecticely [14, 18]. ζ and $m_{eq,1}$, $m_{eq,2}$ are the meshing dampling ratio and the equivalent qulities of pinion and wheel, respectively. γ_i is the phase of the ith pinion relative to the wheel.

Supporting element. As shown in Fig. 4a, the supporting element can be regarded as a coupling element which consists of shaft, bearing and gearbox. In the coupling element, the gear is installed on the shaft and supported by the bearings at both ends of the shaft, and the bearings are mounted on and supported by the gearbox. Therefore, the coupled relationship of shaft-bearing-gearbox can be described by mean of a spring-damper, as demonstrated in

Fig. 4, b. $\mathbf{K}_{bi}$ and $\mathbf{C}_{bi}$ are the supporting stiffness and supporting dampling matrices of bearing supporting point ϵ, respectively. The dynamic model of supporting element can be described as:

$$\mathbf{M}_i\ddot{\mathbf{U}}_i + \mathbf{C}_{bi}\dot{\mathbf{U}}_i + \mathbf{K}_{bi}\mathbf{U}_i = 0, \qquad (6)$$

where: $\mathbf{M}_i$ and $\mathbf{U}_i$ are the mass and vibration displacement matrices of bearing supporting point i, respectively. the helical gear pair meshing matrix. Considering that the influence of the coupling term of $\mathbf{K}_{bi}$ is relatively small, $\mathbf{K}_{bi}$ can be described as Eq. (7), and $\mathbf{C}_{bi}$ has a same structure as $\mathbf{K}_{bi}$ [19].

$$\mathbf{K}_{bi} = diag[k_{xbi}, k_{ybi}, k_{ybi}, k_{\theta bi}], \qquad (7)$$

where: k_{xbi}, k_{ybi}, k_{ybi} and $k_{\theta bi}$ are the bearing supporting stiffness along x-axis, y-axis, z-axis and the torsional stiffness around z-axis of bearing spporting point i, respectivly.

Connecting element. Connecting element is the name of two or more components that play the role of connecting, and it can be equivalent to a spring-damper to describe the coupling relationship between the connecting components, as shown in Fig. 5. $\mathbf{K}_o$ and $\mathbf{C}_o$ are the coupling stiffness and coupling dampling matrix of the coupling nodes $i+1$ and $j-1$, and the connecting element can be described as [20]:
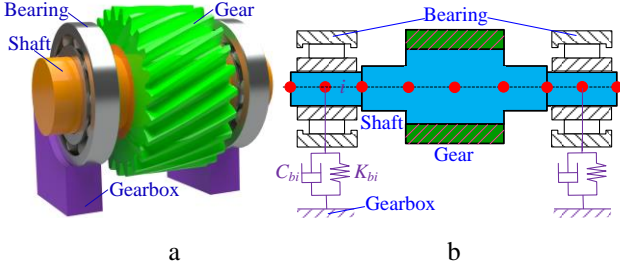

Fig. 4 a) 3D model of shaft-bearing-gearbox element; b) dynamic model of shaft-bearing-gearbox element

$$\begin{bmatrix} \mathbf{M}_{i+1} & \mathbf{0} \\ \mathbf{0} & \mathbf{M}_{j-1} \end{bmatrix}\begin{bmatrix} \ddot{\mathbf{U}}_{i+1} \\ \ddot{\mathbf{U}}_{j-1} \end{bmatrix} + \begin{bmatrix} \mathbf{C}_o & -\mathbf{C}_o \\ -\mathbf{C}_o & \mathbf{C}_o \end{bmatrix}\begin{bmatrix} \dot{\mathbf{U}}_{i+1} \\ \dot{\mathbf{U}}_{j-1} \end{bmatrix} +$$
$$+ \begin{bmatrix} \mathbf{K}_o & -\mathbf{K}_o \\ -\mathbf{K}_o & \mathbf{K}_o \end{bmatrix}\begin{bmatrix} \mathbf{U}_{i+1} \\ \mathbf{U}_{j-1} \end{bmatrix} = 0, \qquad (8)$$

where: $\mathbf{M}_{i+1}$, $\mathbf{M}_{j-1}$ and $\mathbf{U}_{i+1}$, $\mathbf{U}_{j-1}$ are the mass matrices and vibration displacement vectors of the coupling nodes $i+1$ and $j-1$, respectively.
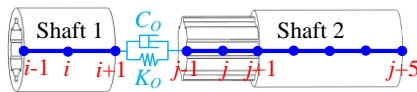

Fig. 5 Dynamic model of connecting element

2.2. Modelling of electric machine

The permanent magnet synchronous motor (PMSM) is widely used in automotive, aviation and other fields due to its high efficiency, fast response and high reliability. The circuit diagram of PMSM under d-q coordinate is shown in Fig. 6, the model of PMSM can be described as [21, 22]:

$$\begin{cases} \dfrac{di_d}{dt} = -\dfrac{R_s}{L_d} \times i_d + \dfrac{L_q}{L_d} \times \omega_r \times i_q + \dfrac{u_d}{L_d} \\ \dfrac{di_q}{dt} = -\dfrac{R_s}{L_d} \times i_d - \dfrac{L_d}{L_q} \times \omega_r \times i_d - \dfrac{\omega_r \times \psi_f}{L_q} + \dfrac{u_q}{L_q} \\ \dfrac{d\omega_r}{dt} = \dfrac{1}{T_M} \times \left[\psi_f \times i_q + \left(L_d - L_q \right) \times i_d \times i_q - T_{load} \right] \\ \dfrac{d\theta_r}{dt} = \omega_r \end{cases}, \quad (9)$$

where: u_d, u_q and i_d, i_q are the components of stator voltage and current on the d-q coordinate, respectively. R_s and L_d, L_q are the stator resistance and the induction on the d-q coordinate, respectively. ω_r, T_M, ψ_f, θ_r and T_{load} are the angular velocity of rotor, mechanical time constant, flux linkage, rotational angular displacement of rotor and load torque, respectively.
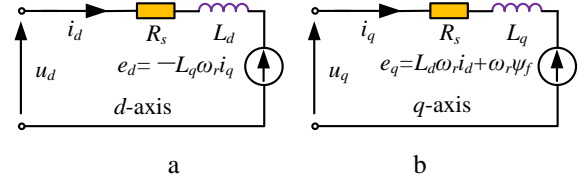

Fig. 6 Circuit diagram of PMSM under d-q coordinate

2.3. Electro-mechanical coupling dynamic model

The dynamic model of MMEDS can be built by means of the shafting element, gear meshing element, supporting element and connecting element based on the assembly relationship and node distribution diagram, as shown in Fig. 7. The whole system is divided into 41 nodes with a total of 164 degrees of freedom. Additionally, considering that the output shaft of the PMSM is coupled with the input shaft of the pinion via coupling, and the gear transmission sub-system of the MMDES is driven by the input torque provided by PMSM. Therefore, the electrical and mechanical parts of the MMDES can be coupled together through torque to establish the ECDM of the MMDES. According to Fig. 7, the input torques T_{mi} ($i = 1, 2, 3$) are applied to the power input nodes 1, 10 and 19, respectively, as the driving moments of the MMDES.
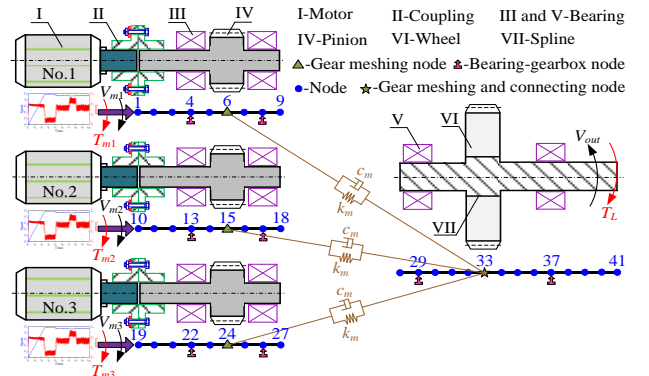

Fig. 7 ECDM of MMEDS and node distribution diagram

The external exciting forces/moments are applied to the load node 41, as the load of the MMDES. Finally, the ECDM of the MMDES can be described as:

$$\mathbf{M\ddot{U} + C\dot{U} + KU = F},\qquad(10)$$

where: **M**, **K**, **C**, **U** and **F** are the whole mass, stiffness, dampling, vibration displacement and external exciting force/moment matrices of the MMDES, respectively. The parameters of PSGS and PMSM are shown Tables 1 and 2, respectively.

Table 1

Parameters of PSGS [11]

	Pinion	Wheel	Unit
No. of tooth	29	180	—
Module	2	2	mm
Width	50	45	mm
Angle of pressure	20	20	$\alpha/°$
Mass	1.03	24.06	Kg
Inertial	4.31E-4	0.41	Kg/m^2
Stiffness of supproting	6.81E7	7.78E7	$Kg.m^2$
Coupling stiffness	$k_x = k_y = k_z = 1.00E10$		Nm^{-1}

Table 2

Parameters of PMSM [11]

	Stator	Rotor	Unit
Resistance	2.882E-1	1.4191E-1	Ω
Rated speed	—	1500	rpm
Volatge	380	—	V
Leakage inductance	3.42E-3	3.42E-3	H
Rotational inertial	—	9.18E-2	$Kg.m^2$
Inertial	4.31E-4	0.41	$Kg.m^2$
Magnetizing inductance	5.733E-2	5.733E-2	H

3. Results and discussion

The load torque acts on the load node 41 is 1200 Nm, and the gear backlash is 50 μm. The speeds of the No.1 and No. 2 PMSMs are the constant value, that is, 1500 rpm. However, the change in the speed of the No. 3 PMSM is shown in Fig. 8. The variation in torque and speed of each PMSM is shown in Fig. 9. Obviously, during 2.5-3.0 s, the averages of the torque and the speed of the PMSMs are about 65 Nm and 1500 rmp respectively, and their fluctuation ranges are [59.63 Nm, 70.69 Nm] and [1499.9, 1500.1] with a relatively small fluctuation proportion. After 3.0 s, the speed of the No. 3 PMSM gradually decreases from 1500 rpm to 1495 rpm, and the RSD (ΔV) is 5 rpm. Because of the three PMSMs are connected to the three pinions via three couplings, and the pinions form a mechanical coupling relationship with the wheel through gear meshing pairs, which produces a forced synchronization effect on the speeds of the PMSMs. As a result, the speeds of the No.1 and No. 2 PMSM also decrease with the speed of the No.3 PMSM decrease. Due to the existence of gear backlash, resulting in the decreasing amplitudes of the speeds of the No.1 and No. 2 PMSMs are significantly less than that of the No.3 PMSM, and the difference between them reach a maximum value of 2 rpm at about 3.77 s. Meanwhile, the driving torque provided by the No. 3 PMSM also begins to decrease little by little, and its value decreases to zero when the time comes to approximately 3.41 s. This is to say, from this moment, the No. 3 PMSM can no longer provide driving torque for the MMDES. Conversely, with the decrease of the torque of the No. 3 PMSM, the torques of the other two PMSMs gradually increase. After 3.77 s, the torque of the No. 3 PMSM starts to increase negatively, which means

the No. 3 PMSM has been converted from the driving state to the load state. Namely, the No. 3 PMSM has been regard as the load by the other two PMSMs, resulting in the torques of the No. 1 and No. 2 PMSMs emerge a positive growth trend. At about 3.84 s (point A), the speeds of the PMSMs reach the same with a value of 1497 rpm. However, the torques of the No. 1 and No. 2 PMSMs corresponding to the point A reach the maximum with a value of 167.1 Nm, and the torque of the No. 3 PMSM corresponding to the point A reach the negative maximum with a value of -145.1 Nm.

Subsequently, the speeds of the PMSMs tend to stabilize after several large fluctuations. In the first stage, the speeds of the PMSMs begin to drop gradually and reach the first trough at about 3.93 s, and the RSD between them reach the maximum with a value of 3 rpm at the first trough. However, the decreasing rate of the speeds of the No. 1 and No. 2 PMSMs is faster than that of the No. 3 PMSM. In the second stage, the speeds of the PMSMs begin to increase slowly and reach the first peak at about 4.12 s, at which time the maximum RSD between PMSMs is slightly reduced and its value is 2 rpm. Meanwhile, the increasing rate of the speeds of the No. 3 PMSM is less than that of the No. 1 and No. 2 PMSMs. At point B, the speeds of all PMSMs reach the same again with a value of 1493 rpm. Correspondingly, compared to the point A, the torques of the No. 1 and No. 2 PMSMs corresponding to the point B has a larger decrease and its value is 133.8 Nm, and a larger increasing of negative tendency can be observed in the torque of the No. 3 PMSM corresponding to the point B and its value is -40.5 Nm. In the third stage, the speeds of the PMSMs begin to drop again and then reach the second trough at about 4.29 s, and the maximum RSD between PMSMs is only 1 rpm at the second trough. The decreasing rate of the speeds of the No. 1 and No. 2 PMSMs is greater than that of the No. 3 PMSM. It can also be seen that the speed curves intersect at point C, and its corresponding speed is 1496 rpm. At point C, the torques of the No. 1 and No. 2 PMSMs is 136.7 Nm with a little change compared to the point B, but the torques of the No. 3 PMSM has a larger change and changes from -40.5 Nm to -99.2 Nm. Finally, due to the action of the mechanical forced synchronization caused by the pinions and the wheel, the speeds of all PMSMs tend to be the same and stabilize at about 1495.35 rpm. That is, the PMSM with a fast speed (namely, No. 1 and No. 2 PMSMs) will be slowed and their speeds reduce from 1500 rpm to 1495.35 rpm with a reduction of 4.65 rpm, and the PMSM with a slow speed (namely, No. 3 PMSM) will be accelerated from 1495 rpm to 1495.35 rpm with an increase of 0.35 rpm. Similarly, the torques of all PMSMs tend to stabilize eventually, as well. The torques of the No. 1, No. 2 and No. 3 PMSMs stabilize at 135.4 Nm, 135.4 Nm and -81.7 Nm, respectively.
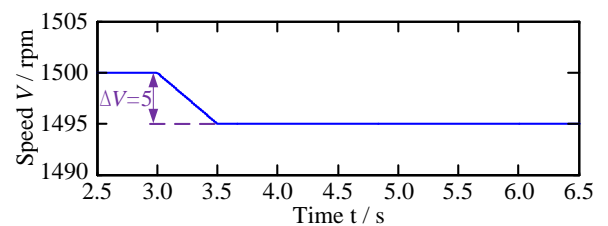
Fig. 8 Speed of PMSM

The dynamic meshing force (DMF) of the pinion-

wheel gear pair is shown in Fig. 10. In Fig. 10, P_i-W represents the gear pair composed of the ith pinion and the wheel. During 2.5-3.0 s, the DMF of the pinion-wheel gear pairs are almost equal to each other, and their mean values are approximately 2856 N. After 3.0 s, due to the change in the speeds of PMSMs, the DMFs of the P_1-W and P_2-W have a positive growth and finally stabilize at about 5794.5 N. Conversely, the DMF of the P_3-W appears a negative increase and decreases to zero at 3.41 s, and then stabilizes at approximately -3513.5 N. This indicates that the 3th pinion has a tendency to disengage from the wheel after 3.0 s and is about to separate from the wheel at 3.41 s, and finally completely disengages from the wheel and maintains back-tooth contact with it.
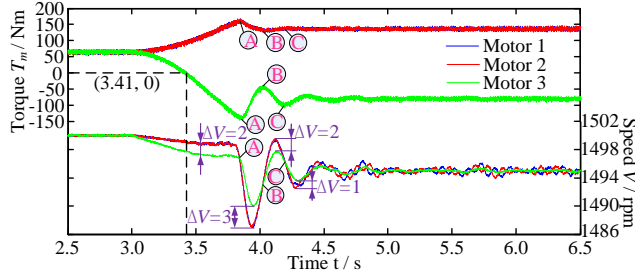
Fig. 9 Torque and speed of PMSM
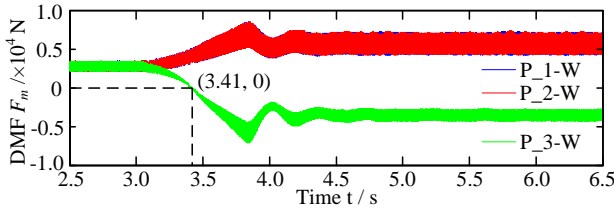
Fig. 10 DMF of the pinion-wheel gear pairs
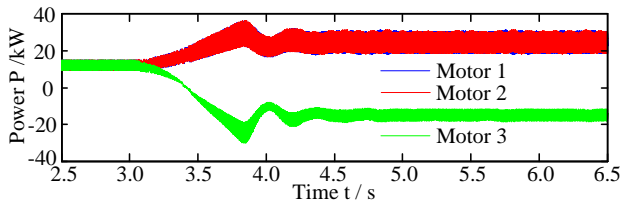
Fig. 11 Output power of each PMSM

The output power of each PMSM is shown in Fig. 11. When the speed of the No. 3 PMSM changes according to the Fig. 8, and its output power reduces from about 12.22 kW to -15.30 kW after experiencing three fluctuations. It means that the No. 3 PMSM does negative work to the system, and the phenomenon of power transfer occurs and its power parasitic amount is 27.52 kW. The generated parasitic power of the No. 3 PMSM is shared by the No. 1 and No. 2 PMSMs equally, so the output powers of the No. 1 and No. 2 PMSMs increases from about 12.22 kW to 25.98 kW respectively. However, the total output power of the PMSMs remains unchanged and its value is approximately 36.66 kW. The variation of the torque and output power of the PMSMs will bound to affect the load-sharing characteristic of the gear transmission system which is measured by the dynamic load-sharing coefficient (DLSC), as shown in Fig. 12. During 2.5-3.0 s, the DLSC is equal 1.0 and varies between 0.855 and 1.131. This also indicates that the DMFs between the pinion-wheel gear pairs are equal to each other, as shown in Fig. 10. After 3.0 s, the DLSCs of

the P_1-W and P_2-W increase gradually and stabilizes at about 1.736 with a fluctuation range of [1.537, 1.935]. However, the DLSC of the P_3-W decreases from 1.0 to -0.572, and the fluctuation range is [-0.8523, -0.2918], which means the load-sharing characteristic of the gear transmission system will be deteriorated when there is an RSD between the PMSMs.
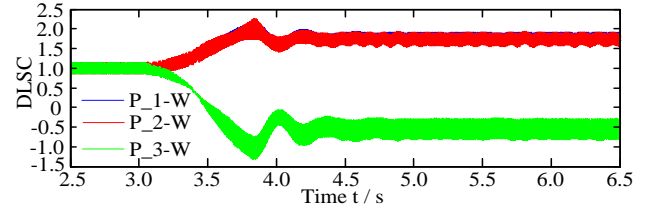

Fig. 12 DLSC of the pinion-wheel gear pairs

The force analysis of pinion-wheel gear pairs is shown in Fig. 13, DMF-Pi (i=1, 2 and 3) represents the DMF acting on the ith pinion, DMF-H is the resultant force of DMF-P1 and DMF-P2. Theoretically, DMF-H and DMF-P3 is equal in size and opposite in direction when $\Delta V = 0$ rpm, resulting in the angles σ between the trajectory lines should be exactly equal, namely σ =120°. In fact, due to the time-varying meshing stiffness and transmission error of gear transmission system, DMF-H and DMF-P3 are no longer equal in size and opposite in direction. That is, the acute angle τ between DMF-H and DMF-P3 is also no longer equal to zero, but $\tau = \delta = 0.0161°$, as shown in Fig. 13, a. As a result, the angles σ will change slightly, and are σ_1 = =119.9963°, σ_2 =119.9904° and σ_3 =120.0133°, respectively, as shown in Fig. 14, a. The maximum angle difference between theoretical angle and simulated angle is $\sigma - \sigma_2 = 0.0096°$, $\sigma_3 - \sigma = 0.0133°$, followed by $\sigma - \sigma_2$ =0.0096° and $\sigma - \sigma_1$ =0.0037°. Geometrically, the trajectory shapes of the pinions are linear. The trajectory line lengths L are also no longer equal to each other, but are $L_1 = 108.00$ μm, $L_2 = 107.94$ μm and $L_3 = 108.02$ μm, respectively. The maximum length difference between the trajectory lines is $L_3 - L_2 = = 0.08$ μm, followed by $L_1 - L_2 = 0.06$ μm and $L_1 - L_3 = = 0.02$ μm. Moreover, as shown in Fig. 15, DMF-Wpi (i=1, 2 and 3) is the DMF of the ith pinion acting on the wheel. δ_1, δ_2 and δ_3 are the angles between DMF-WP1 and y-axis, DMF-WP2 and x-axis, DMF-WP3 and y-axis, respectively. When ΔV =0 rpm, as shown in Fig. 15, a, δ_1 = 45.6225°, δ_2 = 15.6148°, and δ_3 = 155.6188°, respectively. The components of DMF-WP1, DMF-WP2 and DMF-WP3 on the x-axis and y-axis are 2041.32 N and 1997.24 N, -2750.45 N and 768.74 N, 709.40 N and -2766.57 N, respectively. The resultant forces in the x-axis and y-axis are only 0.27 N and -0.6 N, respectively. This means that the vibration equilibrium position (VEP) of the wheel is almost very close to the origin of coordinate, as shown in Fig. 16a, and their offsets in x-axis and y-axis are only 0.014 μm and -0.030 μm, respectively. The offset of the wheel in y-axis nearly twice as much as that in x-axis.

When ΔV =5 rpm, due to the No. 3 PMSM has been regarded as the load by the other two PMSMs, significant changes have been observed in the direction of the DMF-P3, as shown in Fig. 13, b, which makes the acute angle (τ) changes greatly, increasing from 0.0161° to 40.0007°. This will make the angles (σ) also change markedly, and they are σ_1 =60.0050°, σ_2 =60.0063° and σ_3 =120.0113°, respectively, as shown in Fig. 14, b. Compared with when

$\Delta V =0$ rpm, σ_1 has the most obvious change with a decrease of 59.9913°, followed by σ_2 with a decrease of 59.9841°, and the reduction amplitude of σ_3 is minimal, only 0.002°. However, the trajectory shapes of the pinions are still linear. The lengths of the trajectory lines also have a significantly change, and they are $L_1 = 252.41$ μm, $L_2 = 250.22$ μm and $L_3 = 139.42$ μm. The growth in the length is as follows: L_1 has grown by 144.41 μm with a growth rate of 133.71%, L_2 has grown by 142.41 μm with a growth rate of 131.81%, and L_3 has grown by 31.4 μm with a growth rate of 29.07%.
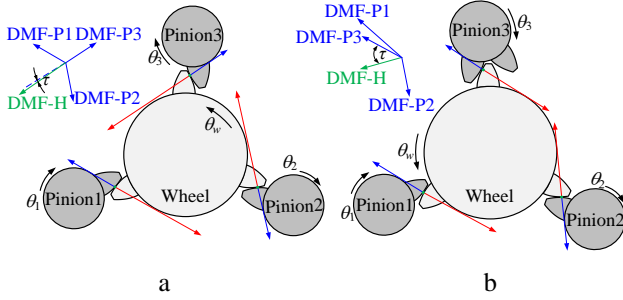
Fig. 13 Force analysis of the pinion-wheel gear pairs: a) when $\Delta V =0$ rpm; b) when $\Delta V =5$ rpm
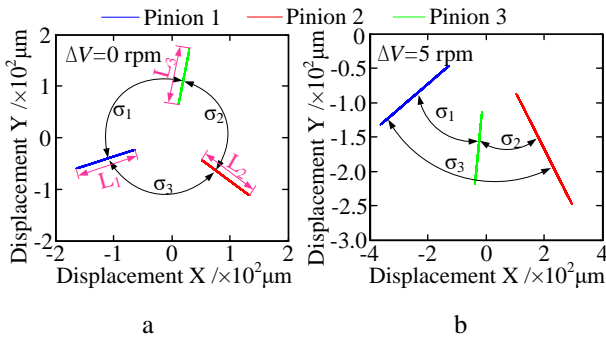
Fig. 14 Trajectories of the pinions: a) when $\Delta V =0$ rpm; b) when $\Delta V =5$ rpm
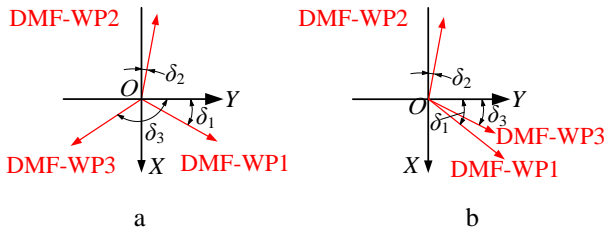
Fig. 15 Force analysis of the wheel: a) when $\Delta V =0$ rpm; b) when $\Delta V = 5$ rpm
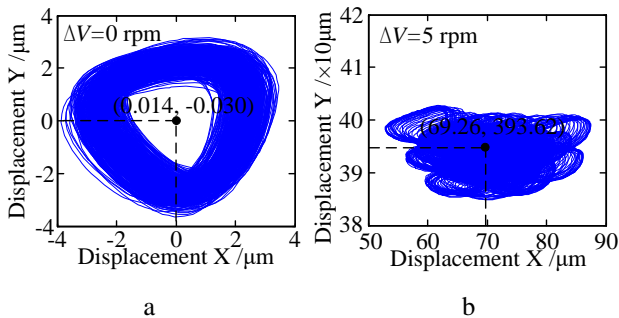

Fig. 16 Motion trajectories of the wheel: a) when $\Delta V = = 0$ rpm; b) when $\Delta V =5$ rpm

Correspondingly, for the wheel, the evidently change can also been observed in the angles δ_1, δ_2 and δ_3. Due to the change in the direction of the DMF-WP3, the change in σ_3 is the largest and decreases from 165.6188° to 35.0007°, with a reduction of 130.6181°, as shown in Fig. 15, b. The change amplitudes in δ_1 and δ_2 are almost the same, increasing from 45.6225° to 55.0057° and from 15.6148° to 24.9989°, with an increase of 9.3832° and 9.8342°, respectively. Similarly, the components of DMF-WP1, DMF-WP2 and DMF-WP3 on the x-axis and y-axis have changed as well, and are 4746.90 N and 3323.58 N, -5251.84 N and 2447.83 N, 2015.29 N and 2878.26 N, respectively. The resultant force in y-axis is almost 5.7 times than that in x-axis, they are 1510.35 N and 8649.67 N, respectively. Aa a consequence, the offset of VEP of the wheel in y-axis is nearly 5.7 times than that in x-axis, and they are 69.26 μm and 393.62 μm, respectively, as shown in Fig. 16, a. In addition, the trajectory shape of the wheel has changed from a relatively regular triangular to an ellipse-like shape, as well. Take the time-frequency characteristic of the DMF of the P_3-W as an example, the effect of the RSD (ΔV) on the dynamic characteristic of MMEDS are analyzed. Fig. 17 shows the time-frequency characteristic of the DMF of the P_3-W when $\Delta V =0$ rpm, f_m and f are the meshing frequency and the rotating frequency, respectively. Obviously, the meshing frequency $f_m = 725$ Hz and its double frequency $2f_m = 1450$ Hz are the dominated frequencies of the DFM of the P_3-W, their amplitudes are 25.89 dB and 16.30 dB, respectively, followed by the frequency $6f = = 150$ Hz and its amplitude is only 5.28 dB.

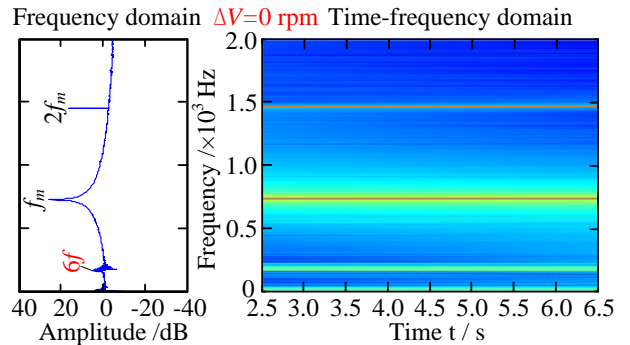Fig. 17 Spectrum of DMF of Pi_3-W when $\Delta V =0$ rpm

The time-frequency characteristics of the DMF of the P_3-W under different ΔV are shown in Fig. 18, the result shows that the meshing frequency f_m and its double frequency $2f_m$ is also the dominated frequencies of the DMF of the P_3-W, and their contributions to their amplitudes vary with ΔV. For example, when $\Delta V=2.5$ rpm, the contributions of f_m and $2f_m$ are 27.15 dB and 17.44 dB, and the rates of contributions are increased by 4.87% and 6.99%, respectively. This indicates that the dominated frequencies of the DMF of the P_3-W do not change with ΔV, but their contributions to their amplitudes change with ΔV. The similar variation law can also be observed in the time-frequency characteristic of the DMF of the P_3-W when $\Delta V=5$ rpm, 7.5 rpm and 10 rpm, respectively. Additionally, the modulation frequencies nf and $mf_m + nf$ (m and $n=1, 2, 3…$) also appear in the spectrum. However, the contributions of the modulation frequencies are significantly less than that of the dominated frequencies.
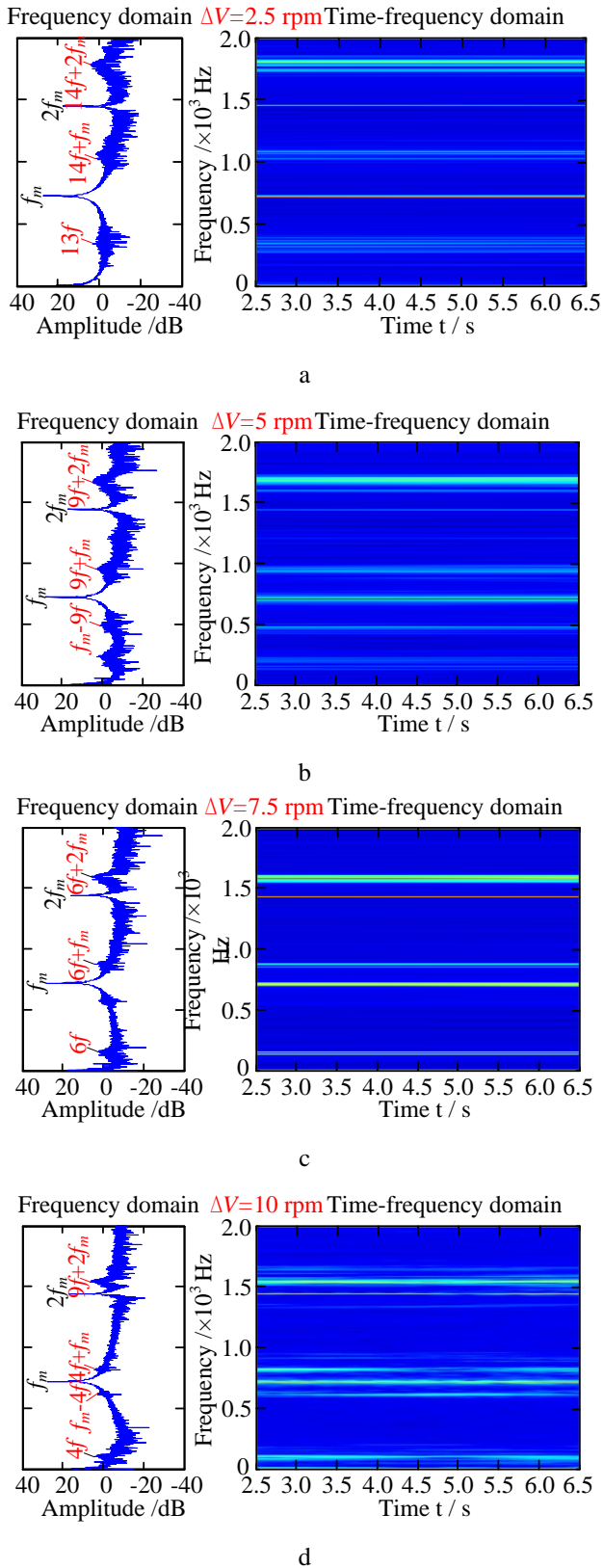
Fig. 18 Spectrum of DMF of Pi_3-W under different ΔV: a) when ΔV =2.5 rpm; b) when ΔV =5 rpm; c) when ΔV =7.5 rpm; d) when ΔV =10 rpm

Fig. 19 shows the phase diagram and poincare map of the wheel in x-direction under different ΔV. When ΔV = 0 rpm, as shown in Fig. 19, a, the trajectories of the lines of the phase diagram do not coincide, but emerges a relatively regular shape. The points in the poincare map are discrete and disorder, but are relatively concentrated. The vibration of the wheel in x-direction can be regarded as a quasi-periodic state. With ΔV increases, as shown in Fig. 19, b to e, the vibration displacement amplitude increases first and then decrease, and are maximum when ΔV=5 rpm. The vibration velocity increases significantly with the increasing of ΔV, which is almost twice as much as when ΔV=0 rpm, and the amplitude of vibration velocity is in the range of [-0.0317 m/s, 0.0243 m/s]. The trajectories of the lines of the phase diagrams still appear to be misaligned, but the shapes of the phase diagrams are still relatively regular. Compared with ΔV=0 rpm, the dispersion degree of the points in the poincare maps increases first and then decreases, and the dispersion degree reaches maximum when ΔV=5 rpm. Meanwhile, the trajectories of the lines of the phase diagrams keep moving as ΔV, and the distribution position of the points in the poincare maps is constantly changing as ΔV, but the vibration state of the wheel in x-direction is basically a quasi-periodic state. This shows that ΔV has a significant effect on the nonlinearity of the vibration of the wheel in x-direction, and the nonlinearity degree first increases and then decreases with ΔV increases.
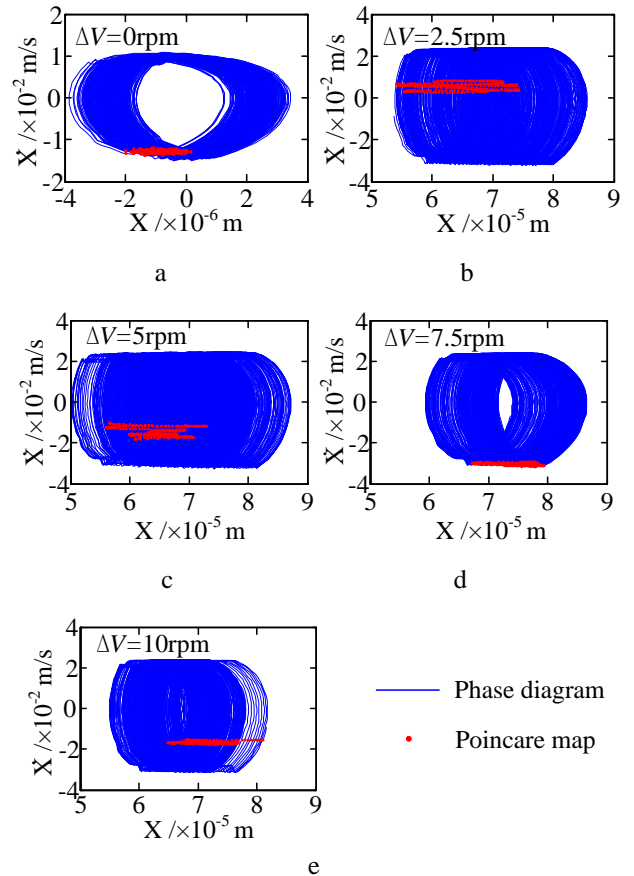

Fig. 19 Phase diagram and poincare map of the wheel in x-direction under different ΔV

The similar variation rule can be observed in the phase diagram and poincare map of the wheel in y-direction, as well, as shown in Fig. 20. Compared with Fig. 19, the effect of ΔV on the vibration displacement amplitude in y-direction is evidently greater than that in x-direction, which can also be verified by the Fig. 21. In Fig. 21, the offsets of the VEP of the wheel in x-direction and y-direction increase with the increase in ΔV, but the offset of the VEP in y-direction is obviously greater than that in x-direction. When
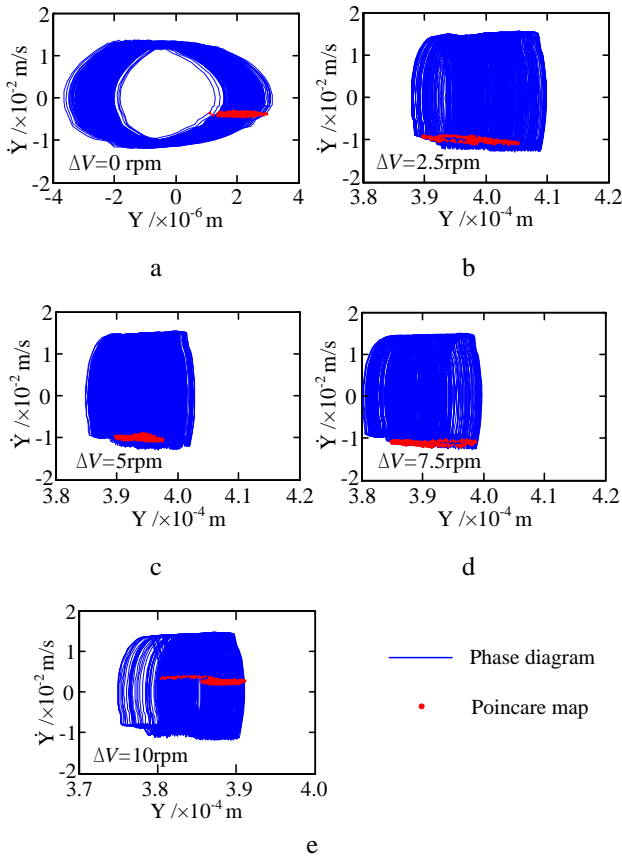
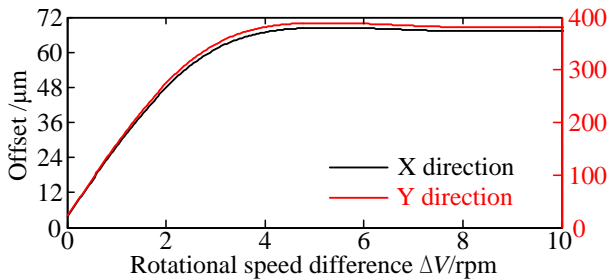Fig. 20 Phase diagram and poincare map of the wheel in y-direction under different ΔV

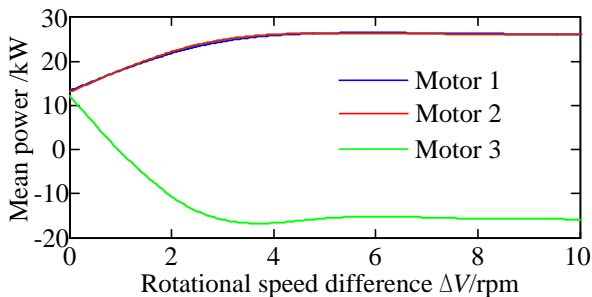Fig. 21 Offset of VEP of the wheel with different ΔV

Fig. 22 Mean power of each PMSM with different ΔV

ΔV≤5 rpm, the growth rate of the offset of the VEP is significantly larger than that when ΔV>5 rpm. The reason is that the sum of the power consumed by the load (namely, 1200 Nm) and the parasitic power transferred by the No. 3 PMSM has exceeded the sum of the maximum output power of the No. 1 and No. 2 PMSMs when ΔV>5 rpm, as shown in Fig. 22. In addition, the vibration velocity in y-direction also increases with the increasing of ΔV, but not signifi-

cantly; compared with ΔV=0 rpm, the range of vibration velocity only increases from [-0.0118 m/s, 0.0136 m/s] to [-0.0127 m/s, 0.0151 m/s]. The other difference with Fig. 19 is that the dispersion degree of the points in the poincare maps has undergone a process of first increasing, then decreasing and finally increasing, and the dispersion degree reaches maximum when ΔV=2.5 rpm.

4. Conclusion

In this paper, a ECDM of MMEDS is set up, including a dynamic model of PSGS and a dynamic model of PMSM. The influence of the forced synchronization action of PSGS on the dynamic characteristics of MMEDS when there is an RSD between motors is discussed. The main results are as follows:

1. When there is an RSD (ΔV) between PMSMs, under the forced synchronization action of PSGS, the PMSM with a fast speed will be slowed and its output torque, output power and the DMF of the corresponding gear pair increases significantly. Conversantly, the PMSM with a slow speed will be accelerated and its output torque, output power and the DMF of the corresponding gear pair decreases markedly. When ΔV≤5 rpm, the increment rate or decrement rate of the output power of PMSM is obviously larger than that when ΔV >5 rpm.

2. Compared with ΔV=0 rpm, when ΔV >0 rpm, the trajectory shape of the wheel has changed from a relatively regular triangular to an ellipse-like shape. The offset of the VEP of the wheel increases with the increase in ΔV, and the growth rate of the offset of the VEP when ΔV≤5 rpm is significantly greater than that when ΔV>5 rpm. In addition, the vibration velocity of the wheel also increases memorably with the increasing of ΔV, but the vibration velocity in y-direction is dramatically less than that in x-direction. Meanwhile, ΔV has a significant effect on the nonlinearity of the vibration of the wheel under the forced synchronization effect of PSGS, and its nonlinearity degree first increases and then decreases with ΔV increases.

3. Compared with ΔV=0 rpm, when ΔV >0 rpm, the dominated frequencies of the DMF of gear pair do not change with ΔV, but their contributions to the amplitude of the DMF change with ΔV. Moreover, the modulation frequencies nf and $mf_m + nf$ (m and n=1, 2, 3…) also appear in the spectrum of the DMF. However, the contributions of the modulation frequencies are significantly less than that of the dominated frequencies.

Conflict of interests

The authors declare that there is no conflict of interests regarding the publication of this paper.

Acknowledgments

References

1. **Chan, C. C.; Bouscayrol, A.; Chen, K.** 2010. Electric, hybrid, and fuel-cell vehicles: architectures and modeling, IEEE Transactions on Vehicular Technology 59: 589-598.
http://doi.org/10.1109/TVT.2009.2033605.

2. **Liu, X. D.; Li, K.; Zhang, C. H.** 2019. Improved backstepping control with nonlinear disturbance observer for the speed control of permanent magnet synchronous motor, Journal of Electrical Engineering & Technology 14: 275-285.
https://doi.org/10.1007/s42835-018-00021-9.

3. **Li, X. H.; Liu, J.** 2012. Harmonic vibration synchronization analysis of the double motors based on equivalent control synchronization strategy, Advanced Materials Research 567: 208-211.
http://doi.org/10.4028/www.scientific.net/AMR.567.208.

4. **Sun, J. W.; Cong, J. Y.** 2022. Optimization and control of vehicle vertical system with suspended in-wheel motor, Mechanika 28(2): 103-112.
http://doi.org/10.5755/j02.mech.30770.

5. **Chen Q. P.** 2014. Study on temperature factors and electromagnetic heat coupling of in-wheel motor micro-electric vehicle, Mechanika 20(1): 80-86.
http://doi.org/10.5755/j01.mech.20.1.6588.

6. **Yu, H. D.; Eberhard, P.; Zhao, Y.; Wang, H.** 2013. Sharing behavior of load transmission on gear pair systems actuated by parallel arrangements of multiple pinions, Mechanism and Machine Theory 65: 58-70.
http://doi.org/10.1016/j.mechmachtheory.2013.02.010.

7. **Li, Z.; Zheng, L.; Gao, W. Y.; Zhan, Z. F.** 2019. Electromechanical coupling mechanism and control strategy for in-wheel motor driven electric vehicles, IEEE Transactions on Industrial Electronics 66(6): 4524-4533.
http://doi.org/10.1109/TIE.2018.2863204.

8. **Wang, W. W.; Li, Y. D.; Shi, J. H.; Lin, C.** 2018. Vibration control method for an electric city bus driven by a dual motor coaxial series drive system based on model predictive control, IEEE Access 6: 41188-41200.
http://doi.org/10.1109/ACCESS.2018.2859356.

9. **Fan, W.; Yang, Y. F.; Su, X. G.** 2020. Dynamic modeling and vibration characteristics analysis of transmission process for dual-motor coupling drive system, Symmetry 12: 1171.
http://doi.org/10.3390/sym12071171.

10. **Wang, D. R.; Yang, F. C.; Jiang, X. F.; Shi, S.; Ma, S. H.** 2022. Electromechanical coupling dynamic characteristics of differential speed regulation system considering inverter harmonics under variable operating conditions, IEEE Access 10: 12057-12069.
http://doi.org/10.1109/ACCESS.2022.3143537.

11. **Shu, R. Z.; Wei, J.; Tan, R. L.; Wu, X. Y.; Fu, B. Y.** 2021. Investigation of dynamic and synchronization properties of a multi-motor driving system: Theoretical analysis and experiment, Mechanical Systems and Signal Processing 153: 107496.
https://doi.org/10.1016/j.ymssp.2020.107496.

12. **Kong, W. K.; Wang, J. X.; Kong, D. W.; Cong, Y. Y. Feng, S. S.** 2021. Motor shifting and torque distribution control of a multi-motor driving system in electric construction vehicles, Advances in Mechanical Engineering 13(6): 1-11.
https://doi.org/10.1177/16878140211028446.

13. **Shi, T. N.; Liu, H.; Geng, Q.; Xia, C. L.** 2016. An improved relative coupling control structure for multi-motor speed synchronous driving system, Iet Electric Power Applications 10(6): 451-457.
https://doi.org/10.1049/iet-epa.2015.0515.

14. **Yang, Y.; Li, M.; Hu, M. H.; Qin, D. T.** 2018. Influence of controllable parameters on load sharing behavior of torque coupling gear set, Mechanism & Machine Theory 121: 286-298.
https://doi.org/10.1016/j.mechmachtheory.2017.10.024.

15. **Fang, P.; Wang, Y. G.; Zou, M.; Zhang, Z. L.** 2021. Combined control strategy for synchronization control in multi-motor-pendulum vibration system, Journal of Vibration and Control 0(0): 1-14.
https://doi.org/10.1177/10775463211007992.

16. **Kahrobaiyan, M. H.; Asghari, M.; Ahmadian, M. T.** 2014. A Timoshenko beam element based on the modified couple stress theory, International Journal of Mechanical Sciences 79: 75-83.
https://doi.org/10.1016/j.ijmecsci.2013.11.014.

17. **Wei, J.; Zhang, A. Q.; Qin, D. T.; Lim, T. C.; Shu, R. Z.; Lin, X. Y.; Meng, F. M.** 2017. A coupling dynamics analysis method for a multistage planetary gear system, Mechanism and Machine Theory 110: 27-49.
https://doi.org/10.1016/j.mechmachtheory.2016.12.007.

18. **Yi, Y. Y.; Qin, D. T.; Liu, C. Z.** 2018. Investigation of electromechanical coupling vibration characteristics of an electric drive multistage gear system, Mechanism and Machine Theory 121: 446-459.
https://doi.org/10.1016/j.mechmachtheory.2017.11.011.

19. **Hu, Z. H.; Tang, J. Y.; Zhong, J.; Chen, S. Y.** 2016. Frequency spectrum and vibration analysis of high speed gear-rotor system with tooth root crack considering transmission error excitation, Engineering Failure Analysis 60: 405-441.
https://doi.org/10.1016/j.engfailanal.2015.11.021.

20. **Shu, R. Z.; Wei, J.; Qin, D. T.; Lim, T. C.; Zhang, A. Q.** 2018. Global sensitivity analysis and dynamic optimization of multi-motor driving transmission system, Structural & Multidisciplinary Optimization 58: 797-816.
https://doi.org/10.1007/s00158-018-1909-3.

21. **Jiang, S.; Li, W.; Wang, Y. Q.; Yang, X. F.; Xu, S. Y.** 2021. Study on electromechanical coupling torsional resonance characteristics of gear system driven by PMSM: a case on shearer semi-direct drive cutting transmission system, Nonlinear Dynamics 104: 1205-1225.
https://doi.org/10.1007/s11071-021-06364-9.

22. **Qiao, Z. W.; Shi, T. N.; Wang, Y. D.; Yan, Y.; Xia, C. L.; He, X. N.** New sliding-mode observer for position sensorless control of permanent-magnet synchronous motor, IEEE Transactions on Industrial Electronics 60: 710-719.
https://doi.org/ 10.1109/TIE.2012.2206359.

R. Shu, Z. Xie, S. Ge, Q. Yin, Z. Zou, R. Tan, J. Fu

RESEARCH ON DYNAMIC CHARACTERISTICS OF A MULTI-MOTOR ELECTRIC DRIVING SYSTEM CAUSED BY PARASITIC POWER

S u m m a r y

To reduce greenhouse gas emissions in dealing with climate change, replacing fuel vehicles with electric vehicles (EVs) is one of the most effective measures. The multi-motor electric drive system (MMEDS), which is widely used in EVs, is driven by two or more permanent magnet synchronous motors (PMSM) by parallel shaft gear set (PSGS). Due to the action of forced synchronization of PSGS, once there is a rotational speed difference (ΔV) between PMSMs, this will break the balance of output power between PMSMs and cause the increase in output power of some PMSMs while others decrease or even become negative, and eventually generate parasitic power. Parasitic power in MMEDS is bound to cause an auto excitation vibration and a variation in dynamic characteristics of MMEDS. Therefore, in this paper, an electro-mechanical coupled dynamic model of MMEDS is set up, including a dynamic model of PSGS and a dynamic model of PMSM.

Then, the affect of the forced synchronization action of PSGS on the dynamic characteristic of MMEDS is investigated under different ΔV. The results show that under the action of the forced synchronization of PSGS, the output power of the PMSM with a fast speed (or a slow speed) increase (or decreases) with the increasing of ΔV, and when $\Delta V \leq 5$ rpm, the increment rate or decrement rate of the output power of PMSM is obviously greater than that when $\Delta V > 5$ rpm. Meanwhile, ΔV has a significant effect on the nonlinearity of the vibration of the wheel, which increases first and then decreases with ΔV increases. The dominated frequencies of dynamic meshing force (DMF) of gear pair do not change with ΔV, but their contributions to the amplitude of the DMF change with ΔV. Moreover, the modulation frequencies also appear in the spectrum of the DMF, but their contributions to the amplitude of the DMF are significantly less than that of the dominated frequencies.